PNAS
www.pnas.org

Supporting Information for

Dual-axial Engineering on Atomically Dispersed Catalysts for Ultrastable Oxygen Reduction in Acidic and Alkaline Solutions

Meng Dan,[ab] Xiting Zhang,[a] Yongchao Yang,[c] Jingfei Yang,[a] Fengxiu Wu,[a] Shenlong Zhao,*[c] Zhao-Qing Liu*[a]

*Shenlong Zhao
Email: shenlong.zhao@sydney.edu.au
*Zhao-Qing Liu
Email: lzqgzu@gzhu.edu.cn

This PDF file includes:

Supporting Information Text

Experimental details

Preparation of catalysts. All chemicals with analytical grade were used as received without further purification. The ZIF-8 and Co-ZIF-8 were synthesized by a simple solvothermal method. Concretely, 2-methylimidazole (16 mmol) was dissolved in 15 mL methanol under stirring in flask A. $Zn(NO_3)_2{\cdot}6H_2O$ (4 mmol) was dissolved in 30 mL methanol to form a clear solution in flask B. The solution in flask B was subsequently added into flask A under vigorous stirring (1000 rpm) for 1 h. The solution was transferred into a 100 mL Teflonlined stainless-steel autoclave and heated at 120 °C for 4 h. The product was separated by centrifugation, washed with methanol for five times and finally dried at 70 °C under vacuum overnight. Similarly, the Co-ZIF-8 was synthesized except that the 0.4 mmol $Co(NO_3)_2{\cdot}6H_2O$ was also added into flask B. The Co/CN, Co/DACN and the controlling samples were prepared via pyrolysis. The as-obtained ZIF-8 or Co-ZIF-8 was transferred into a quartz boat and placed in a tube furnace, heated to the desired temperature at a rate of 5 °C·min^{-1} under flowing Ar gas with a dwell time of 3 h, and then naturally cooled to room temperature. Concretely, the Co/CN and Co/DACN were prepared by pyrolysis of Co-ZIF-8 precursor at 900 and 950 °C (above the boiling point of Zn (907 ºC)) (1,2), respectively. The Zn/CN was synthesized with ZIF-8 as precursor at 900 °C for comparison.

Materials characterizations. Scanning electron microscopy (SEM) images were taken on a JEOL JSM-7600F microscope. Transition electron microscopy (TEM) measurements were conducted on ThermoFisher Talos F200X (FETEM) operated at 200 kV. HAADF-STEM images were taken using a convergence semi-angle of 11 mrad with inner and outer collection angles of 59 and 200 mrad, respectively. The corresponding EDS mapping was conducted using 4 in-column Super-X detectors. X-ray diffraction (XRD) patterns were recorded with a Panalytical X'Pert Pro X-ray Powder Diffractometer using Cu Kα radiation. The D- and G- bands of the carbon in the pyrolyzed samples were analyzed by Raman spectroscopy on a HORIBA JobinYvon with a 514 nm laser acting as an excitation source. The N_2 adsorption-desorption isotherms and pore-size distributions were determined at 77 K with a Quadrasorb SI analyzer. The Brunauer-Emmett-Teller (BET) method was utilized to calculate the specific areas of the samples. X-ray photoelectron spectroscopy (XPS) was measured on a PHI5300 spectrometer with a Kratos Axis Ultra DLD electron detector. All XPS calibrations were referenced to the surface adventitious carbon at 284.8 eV. The elemental compositions were measured by inductively coupled plasma atomic emission spectroscopy (ICP-AES) on a Varian ES.
X-ray absorption spectra (XAS), including X-ray absorption near-edge structure (XANES) and extended X-ray absorption fine structure (EXAFS) of the samples at Co K-edge (7.69 - 7.79 keV) and Zn K-edge (9.64 - 9.73 keV) were collected in transmission mode at the Singapore Synchrotron Light Source (SSLS) center, where a pair of channel-cut Si (111) crystals was used as the monochromator. The storage ring was working at the energy of 2.5 GeV with an average electron current below 200mA. The EXAFS data were extracted and fitted according to the standard procedures using the ATHENA module implemented in the FEFF6.0 software packages (3). The k^3-weighted Fourier transform (FT) of x (k) in *R* space was obtained over an *R*-range of 0-14.0 Å^{-1} by applying a Besse window function.

Electrochemical measurements. Electrochemical measurements were performed using a standard three-electrode system on an electrochemical workstation (Princeton Applied Research model: 636 A). Hg/HgO and Hg/HgCl electrodes were used as the reference electrode in alkaline and acidic media, respectively, a carbon rod as the counter electrode, and a glassy-carbon Rotating Ring-Disk Electrode (RRDE, 5 mm in diameter) as the working electrode. Cyclic voltammetry (CV) and linear sweep voltammetry (LSV) curves were obtained in an O_2- or N_2-saturated 0.1 M KOH solution. Prior to electrochemical measurements, 4.9 mg of the catalyst was dispersed in a mixture of 300 µL DI water, 700 µL ethanol and 20 µL Nafion solution, followed by ultrasonication for 30 min to prepare catalyst ink. Subsequently, 10 µL of a catalyst ink was transferred onto the RRDE.
Before the ORR test, CVs in O_2-saturated 0.1 M KOH or 0.5 M H_2SO_4 were performed at 50 mV s^{-1} for at least 10 cycles to clean and stabilize the catalyst surface. And then, LSVs of the ORR measurements were conducted in 0.1 M KOH or 0.5 M H_2SO_4 purged with O_2 (saturated) at a scan rate of 10 mV s^{-1} and a rotation rate of 1600 rpm. The durability of the catalyst was evaluated by the Chronoamperometric (CA) method in O_2-saturated 0.1 M KOH or 0.5 M H_2SO_4 at a constant potential of 0.60 V vs. RHE. The electron transfer number (*n*) and the yield of peroxide (*y*) were calculated from the disk current (I_{Disk}) and ring current (I_{Ring}) during the RRDE measurements using the following Eqs. (1) and (2):

$$n = 4I_{Disk}/(I_{Disk}+I_{Ring}/N) \quad (1)$$

$$y(\%) = (200\times I_{Ring}/N)/(I_{Disk}+I_{Ring}/N) \quad (2)$$

where N = 34% is the current collection efficiency of the Pt ring.

The electrochemically active surface area (ECSA) was estimated by the double-layer capacitance (C_{dl}) via CVs in a non-Faradaic potential region at scan rates ranging from 5 to 50 mV s^{-1} in 0.1 M KOH. The ECSA was calculated from the corresponding C_{dl}, based on Eq. (3):

$$ECSA = C_{dl}/C_s \quad (3)$$

The C_{dl} was calculated as the double-layer charging current divided by the scan rate ($C_{dl} = i_c/v$). The C_s is the specific capacitance, reported to be similar in the same aqueous electrolyte (4).
The mass and specific activities were calculated using Eqs. (4) and (5):

$$\text{Mass activity}(mA/mg_{metal}) = j_k/\text{catalyst loading}(mg_{metal}/cm^2) \quad (4)$$

$$\text{Specific activity}\ (mA/cm^2_{ECSA}) = \text{mass activity/ECSA}\ (cm^2/mg_{catalyst}) \quad (5)$$

where j_k is the kinetic current density according to the Koutecky–Levich equation.
All the measured potentials against the Hg/HgO were converted to the reversible hydrogen electrode (RHE) using the equation: $E(RHE) = E(Hg/HgO) + 0.0591pH + 0.098$ V.
All the measured potentials against the $Hg/HgCl_2$ were converted to the reversible hydrogen electrode (RHE) using the equation: $E(RHE) = E(Hg/HgCl_2) + 0.0591pH + 0.241$ V.

ZAB measurements. The performance testing of the catalysts in rechargeable ZABs was conducted using homebuilt electrochemical cells. All data were collected using a CHI 760D (CH Instruments, Inc., Shanghai, China) electrochemical workstation at room temperature. Zinc foil was used as the metal anode, and the air electrode was fabricated using a Nafion-coated carbon fiber paper loaded with 3.0 mg Pt/C and 3.0 mg catalyst. For comparison, a gas diffusion layer loaded with 3.0 mg Pt/C and 3.0 mg IrO_2 was used as the air electrode. For all ZABs, an aqueous 6.0 M KOH solution was used as the electrolyte.

DFT calculations. First-principle calculations were performed with the Vienna *Ab Initio* Simulation Package (VASP, version 5.4), utilizing a generalized gradient approximation (GGA) with the Perdew-Burke-Ernzerhof (PBE) exchange and correlation functions (5, 6). A plane-wave basis set with a cut-off energy at 400 eV within the framework of the projector-augmented wave method was used (7,8). The Brillouin zone was sampled with 3 × 3 × 1 K points. The vacuum space was set to 15 Å to avoid the interaction between neighboring lattices. All atoms were converged to 0.01 eV/Å. The geometry optimization convergence tolerance of energy and the force were set to 1.0×10^{-4} eV/atom and 0.03 eV/Å, respectively. The spin polarization was considered in all calculations.
Adsorption energies of gas molecules were calculated by the Eq. (6):

$$E_{ads} = E_{tot}–(E_{catal}+E_{mol}) \quad (6)$$

where E_{tot}, E_{catal}, and E_{mol} refer to the DFT calculated total energy of the adsorption complex, the catalyst structures and the isolated molecules, respectively.
The free energies of ORR species (ΔG) can be expressed as the Eq. (7):

$$\Delta G = E_{ads} + \Delta E_{ZPE} – T\Delta S \quad (7)$$

where ΔE_{ZPE} and $T\Delta S$ refer to zero-point energy correction and entropic energy, respectively, the free energy of ($H^+ + e^-$) at standard conditions is assumed to be 1/2 H_2 (9).

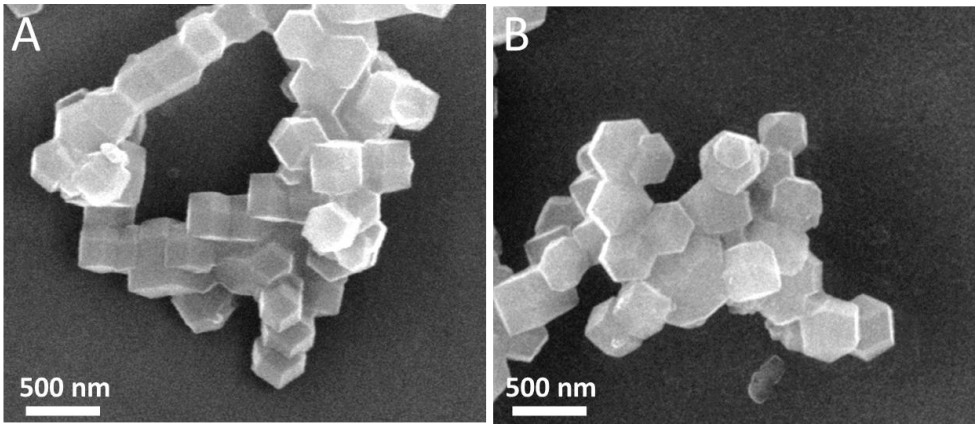

Fig. S1. SEM images of (A) ZIF-8 and (B) Co-ZIF-8. The ZIF-8 and Co-ZIF-8 exhibited similar morphology with rhombic dodecahedron shape.

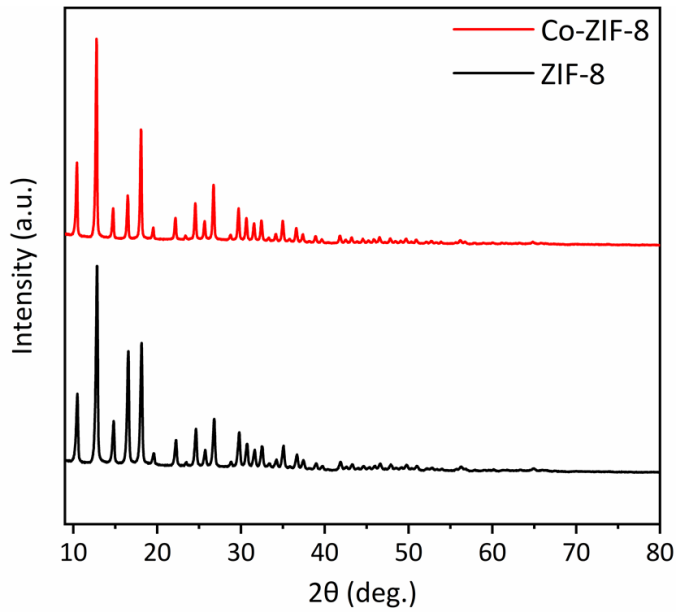

Fig. S2. XRD patterns of ZIF-8 and Co-ZIF-8. The XRD patterns of ZIF-8 can be still maintained with the introduction of Co.

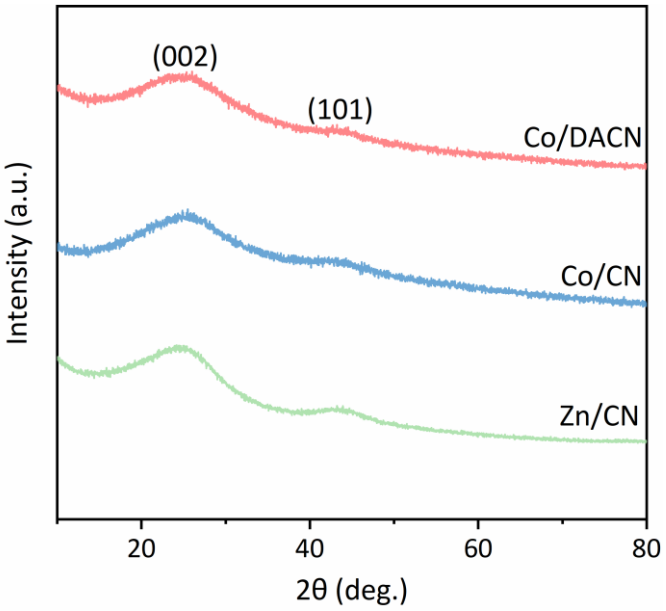

Fig. S3. XRD patterns of Zn/CN, Co/CN and Co/DACN.

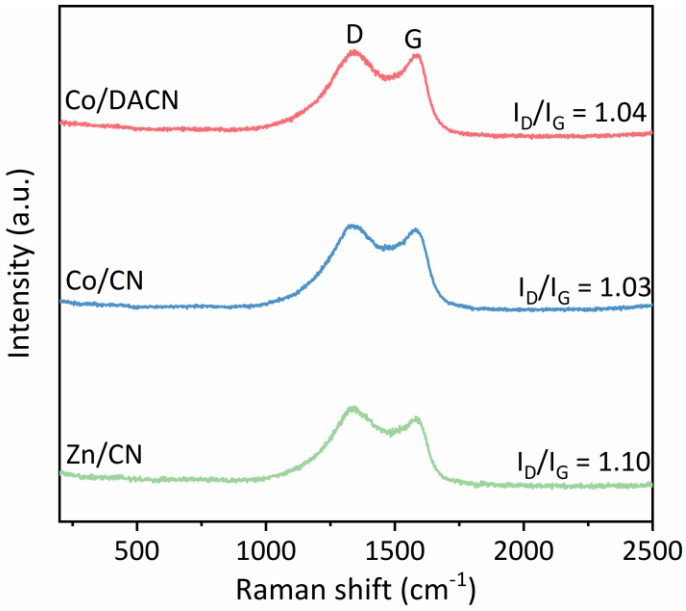

Fig. S4. Raman spectra of the Zn/CN, Co/CN and Co/DACN.

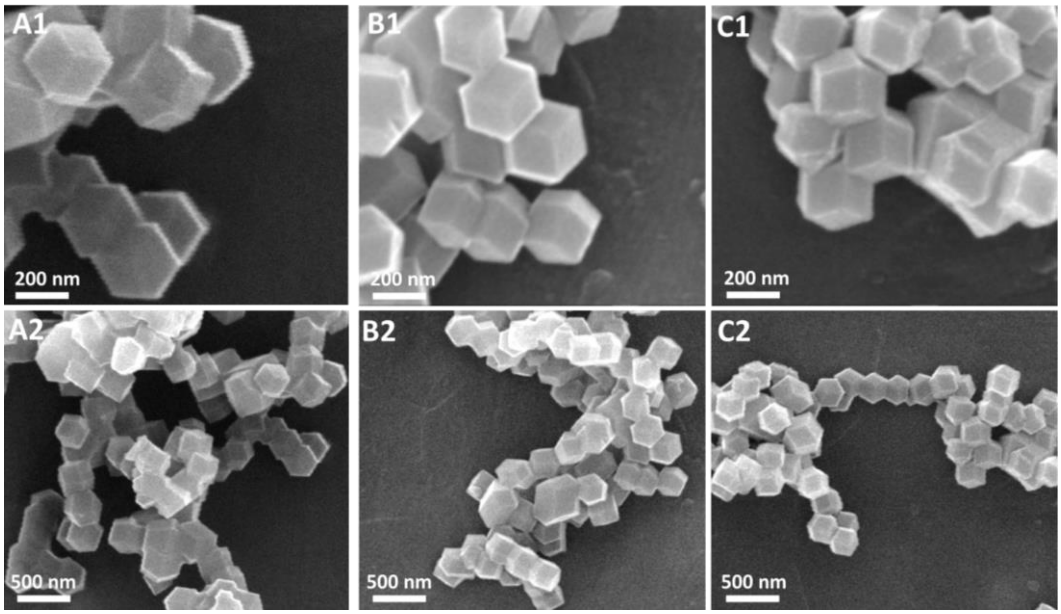

Fig. S5. SEM images of (A) Zn/CN, (B) Co/CN, (C) Co/DACN at high and low magnifications.

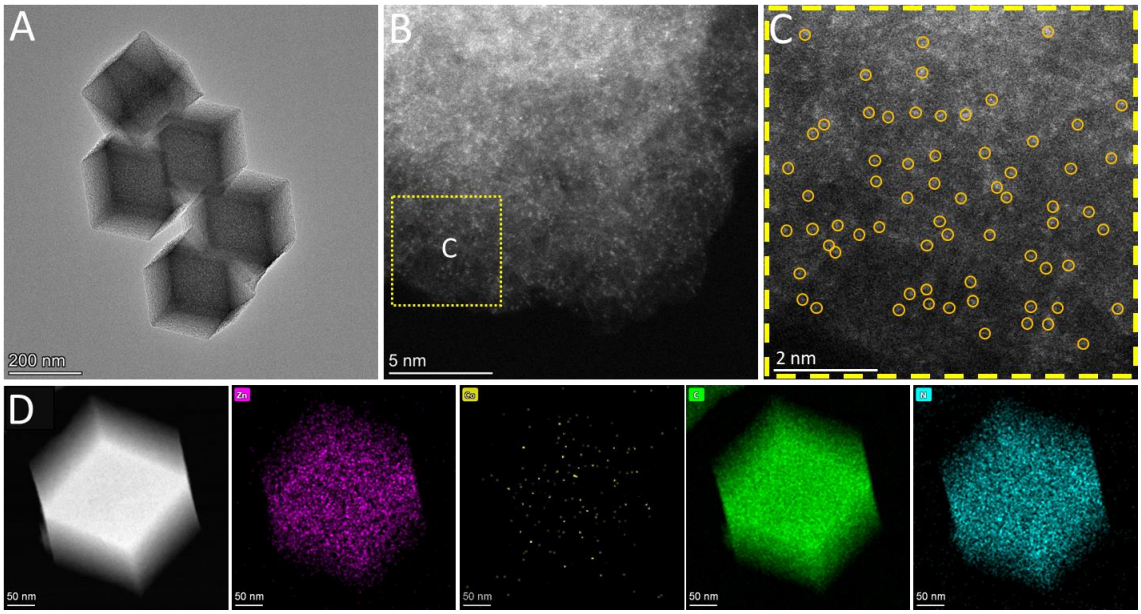

Fig. S6. Microscopic characterization of Zn/CN. (A) TEM images, (B, C) HAADF-STEM images, (D) STEM image and the corresponding elemental distributions of Zn (purple), Co (yellow), C (green), and N (blue).

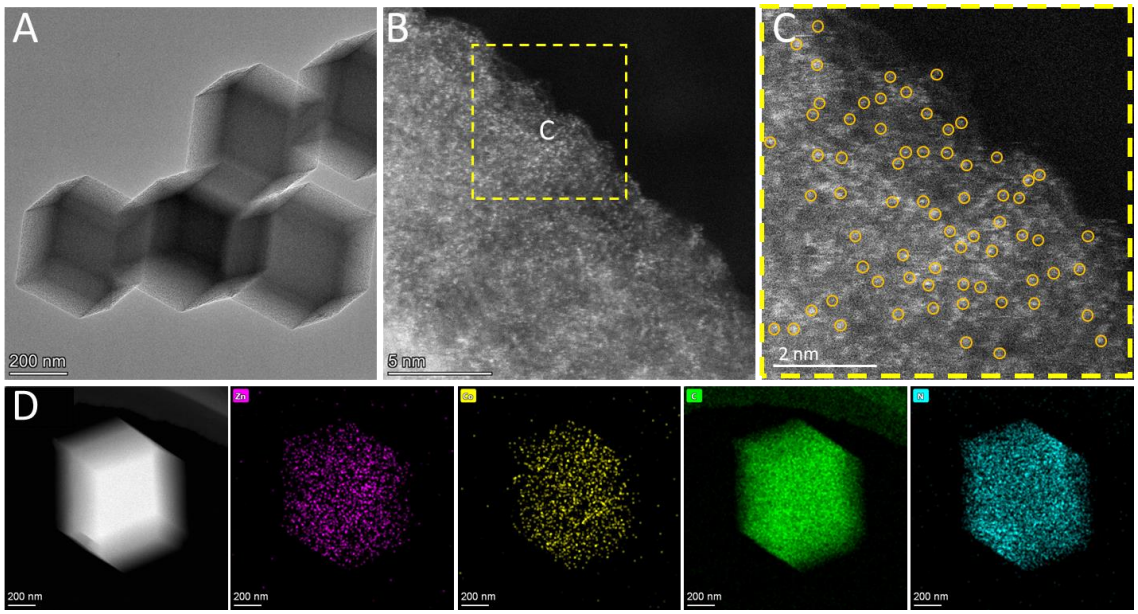

Fig. S7. Microscopic characterization of Co/CN. (A) TEM images, (B, C) HAADF-STEM images, (D) Scanning transmission electron microscopy (STEM) image and the corresponding elemental distributions of Zn (purple), Co (yellow), C (green), and N (blue).

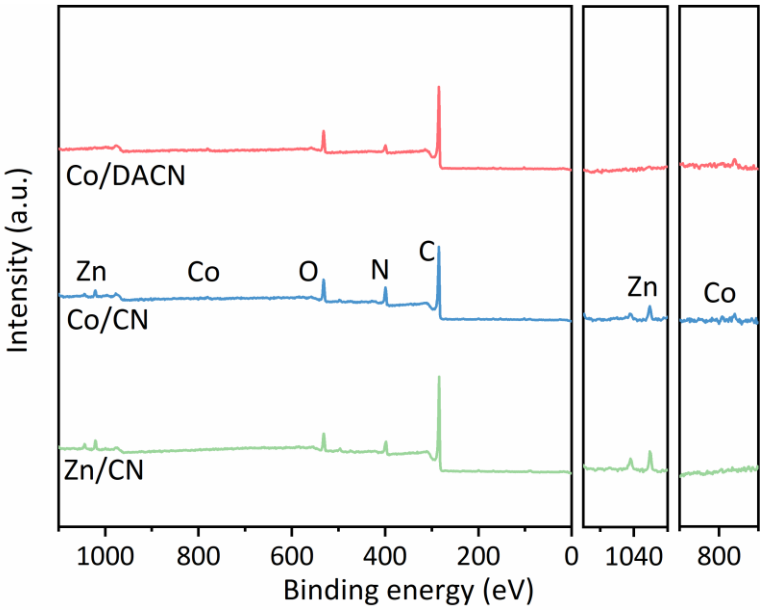

Fig. S8. XPS survey spectra of Zn/CN, Co/CN and Co/DACN catalysts.

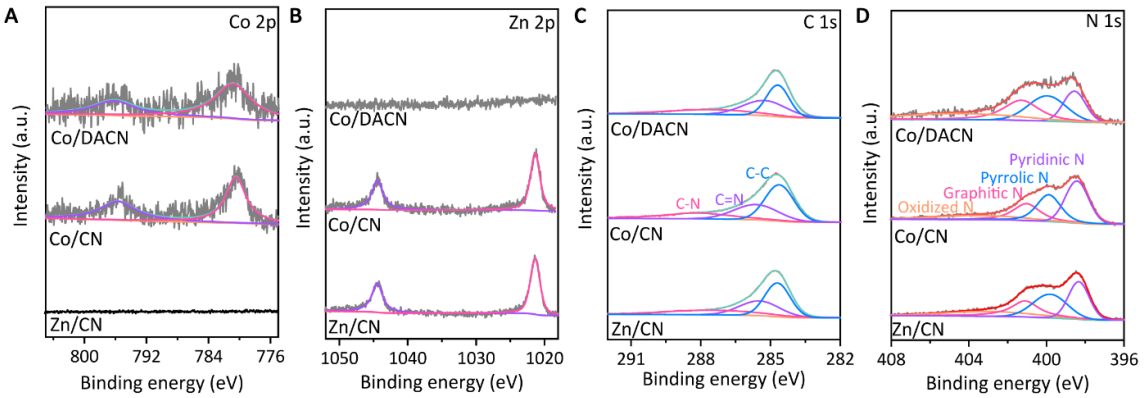

Fig. S9. High resolution XPS spectra of (A) Co 2p, (B) Zn 2p, (C) C 1s, and (D) N 1s for Zn/CN, Co/CN and Co/DACN. In Co 2p XPS spectra, the peak of Co $2p_{3/2}$ was located at 780.45 and 780.88 eV for Co/CN and Co/DACN, respectively, which centered between 778.1-778.8 eV (Co^0) and 780.9 eV (Co^{2+}). Therefore, the chemical valence of Co was close to +2 in these samples. The peak of Zn $2p_{3/2}$ was located at about 1021.3 eV for Zn/CN and Co/CN, respectively, different from that (1022.0 eV) for ZnO and metal Zn^0 (1020.8 eV).

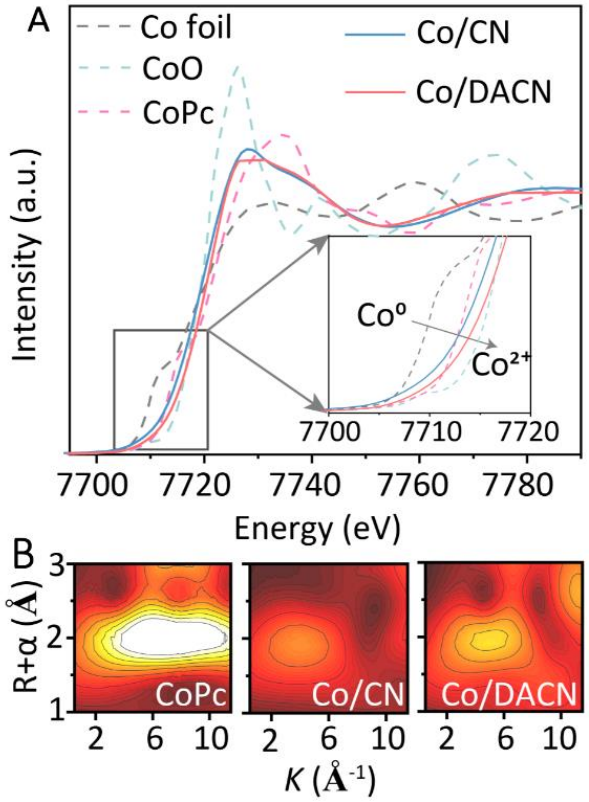

Fig. S10. a) Normalized XANES spectra at Co K-edge for Co/CN, Co/DACN, and reference samples, b) WT-EXAFS contour plots at Co K-edge for Co/CN, Co/DACN and the reference CoPc.

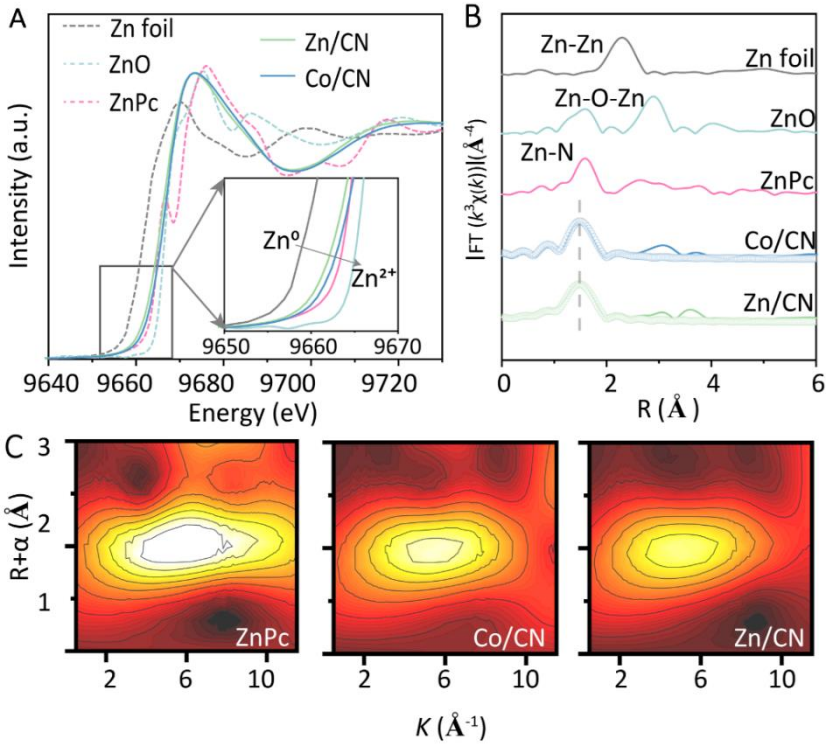

Fig. S11. a) Normalized XANES spectra, b) FT-EXAFS spectra and fitting curves at Zn K-edge for Zn/CN, Co/CN, Co/DACN, and reference samples, c) WT-EXAFS contour plots at Zn K-edge for Zn/CN, Co/CN, Co/DACN, and the reference ZnPc. The K-edge XANES spectra of Zn (Fig. S11a) supported that the valence state of Zn was between 0 and +2, which was consistent with the XPS results (Fig. S8, 9 and Tables S3-5). The Fourier transform k^3-weighted EXAFS (FT-EXAFS) spectra showed that the coordination environment of Zn was similar to that of zinc phthalocyanine (ZnPc) with the main peak at around 1.60 Å corresponding to the scattering path of Zn-N bond rather than Zn-Zn bond (Fig. S11b). Wavelet transform (WT) was also employed to investigate the Zn K-edge EXAFS oscillations of Zn/CN and Co/CN. Only one intensity maximum was located at about 5.4 $Å^{-1}$ which was close to that in the reference ZnPc.

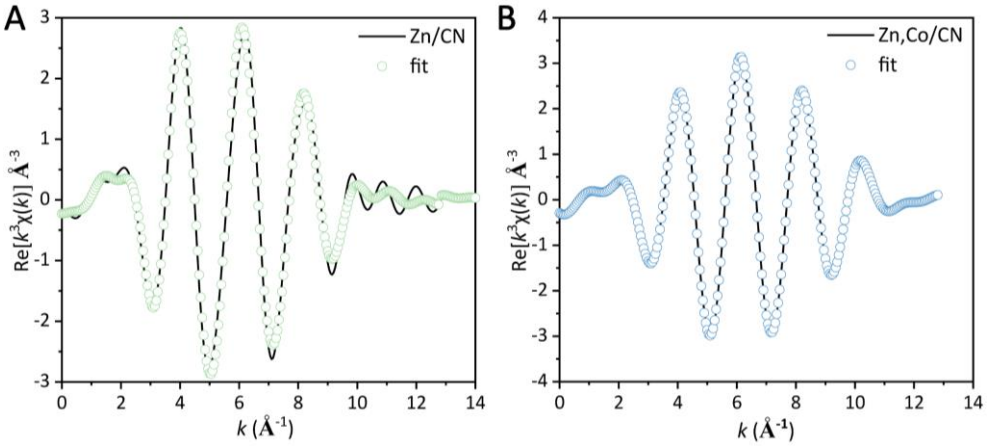

Fig. S12. Zn K-edge EXAFS spectra in k space for a) Zn/CN and b) Co/CN.

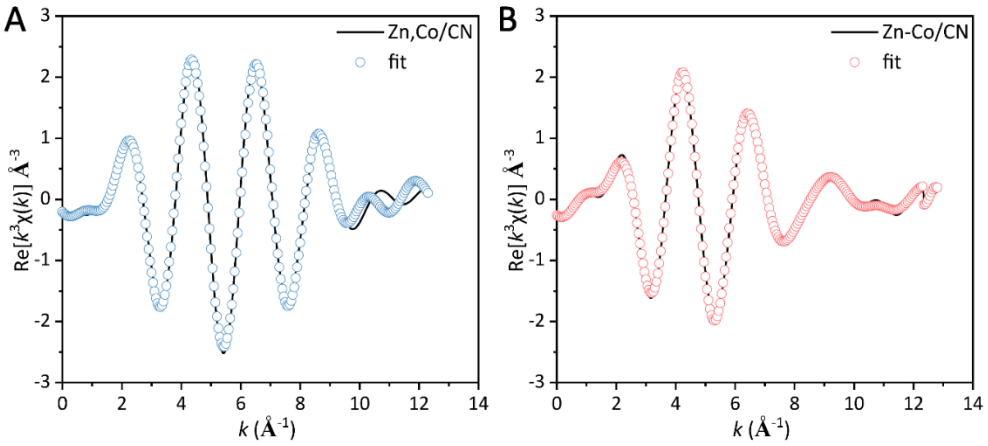

Fig. S13. Co K-edge EXAFS spectra in k space for a) Co/CN and b) Co/DACN.

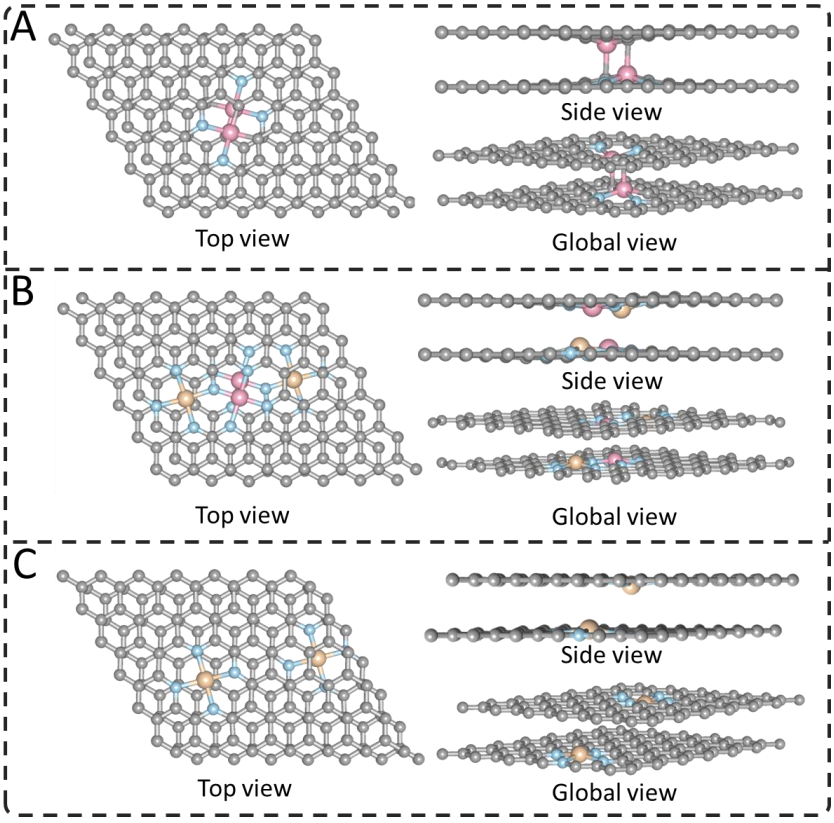

Fig. S14. Optimized calculation models for a) Co/DACN, b) Co/CN and c) Zn/CN.

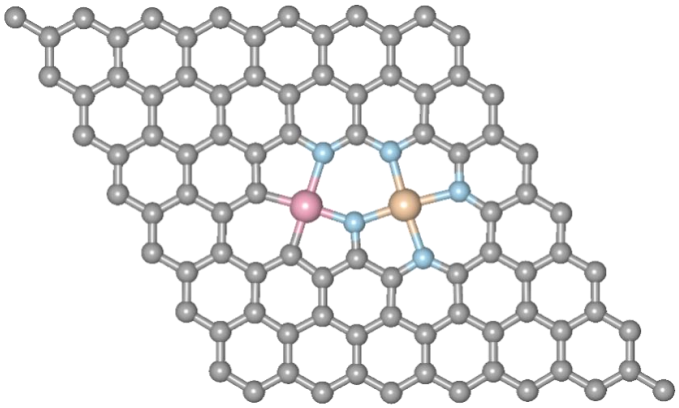

Fig. S15. Optimized theoretical models for Co/DACN-S, the Co/DACN-S with single layer Co/DACN structure.

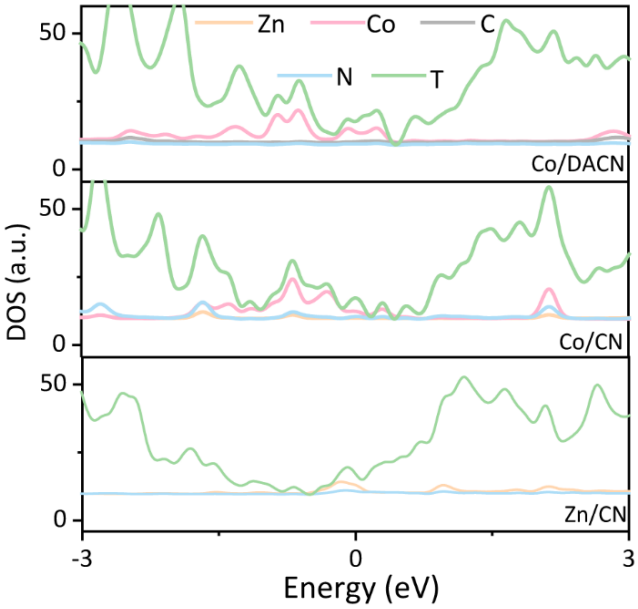

Fig. S16. Density of states (DOS) of Zn/CN, Co/CN and Co/DACN.

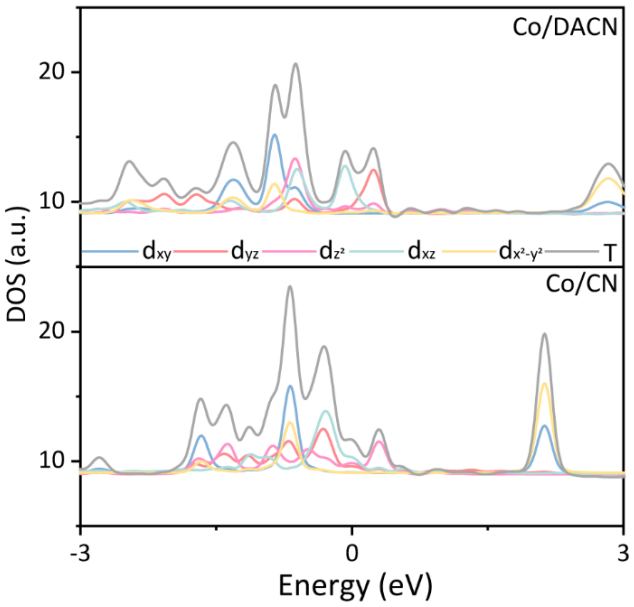

Fig. S17. DOS of 3d orbitals of Co in Co/CN and Co/DACN.

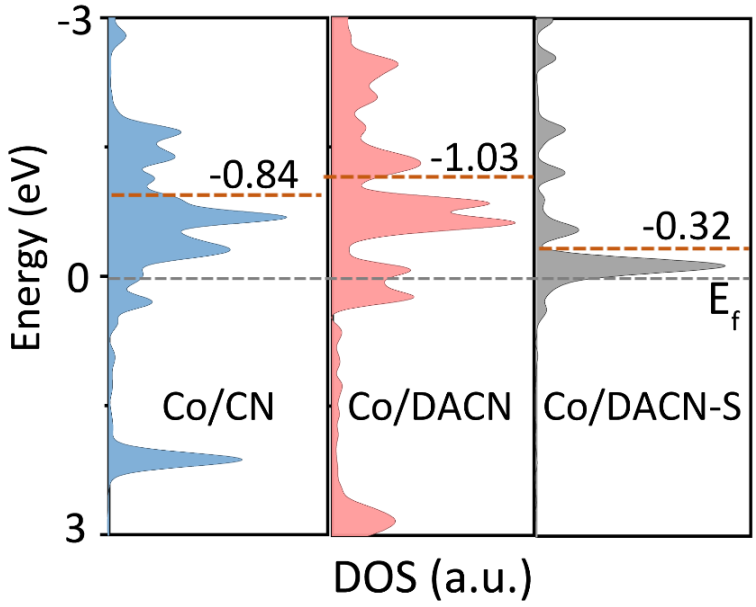

Fig. S18. The d-band centers of Co atom in all-obtained catalysts.

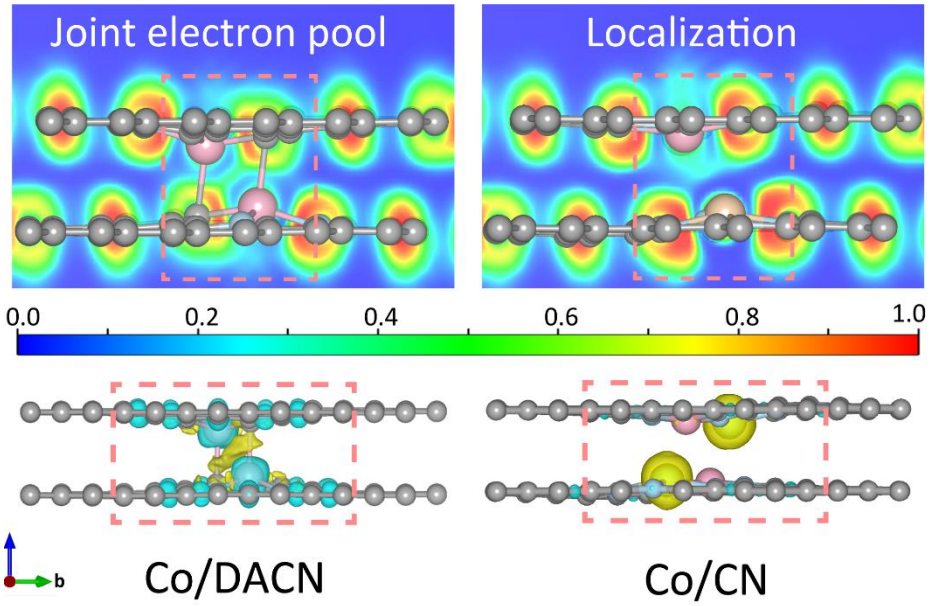

Fig. S19. Electron location function (ELF) and charge density plots of Co/CN and Co/DACN, whereas the charge accumulation and depletion are represented in blue and yellow regions, respectively.

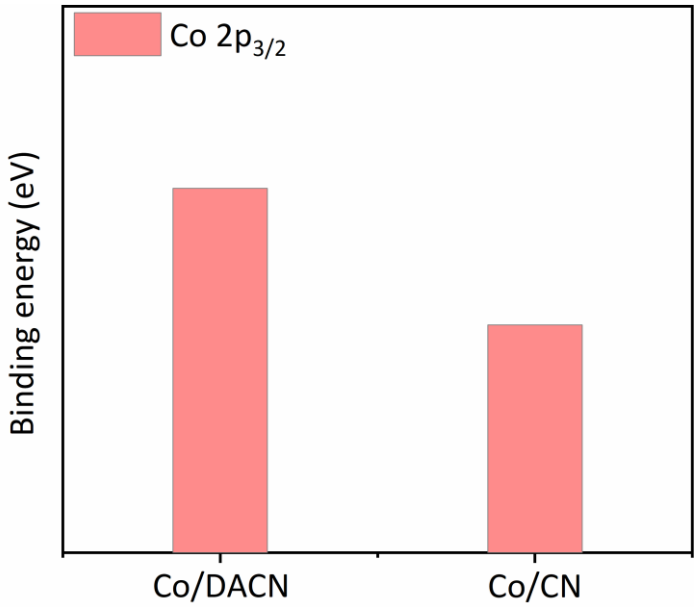

Fig. S20. The binding energies of Co $2p_{3/2}$ from XPS studies.

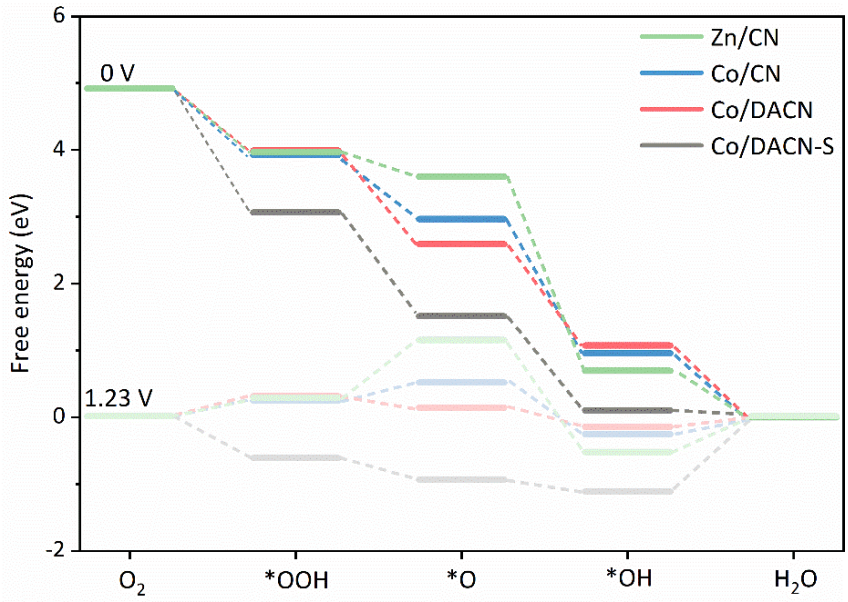

Fig. S21. Calculated free energy diagram of ORR on the different samples at 0 and 1.23 V.

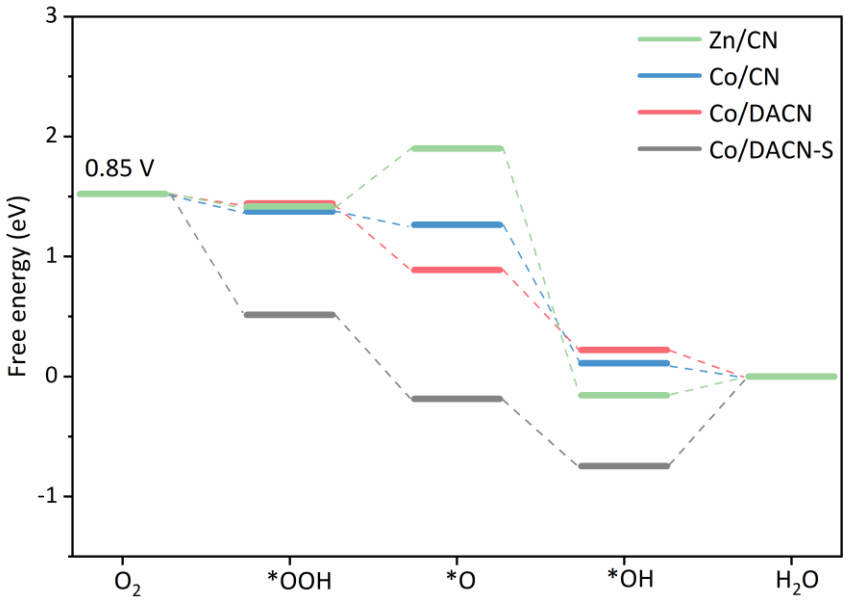

Fig. S22. Calculated free energy diagram of ORR on the different catalysts at 0.85 V.

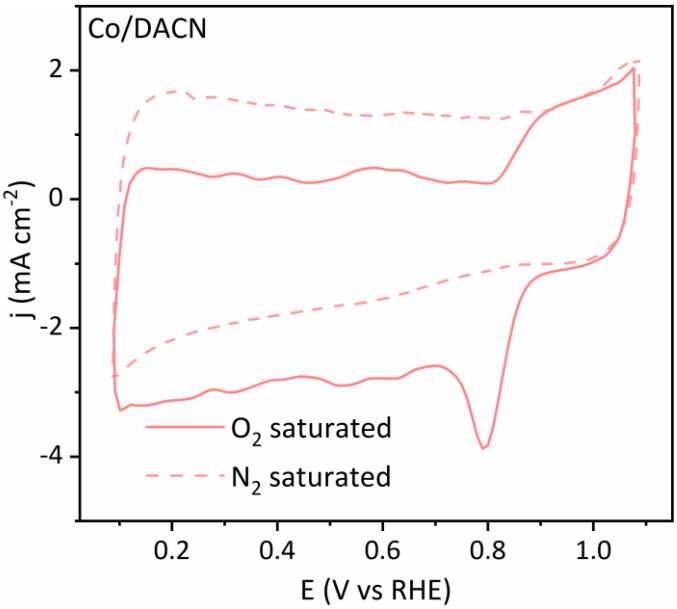

Fig. S23. CV curves of Co/DACN in O_2- or N_2-saturated 0.1 M KOH solution.

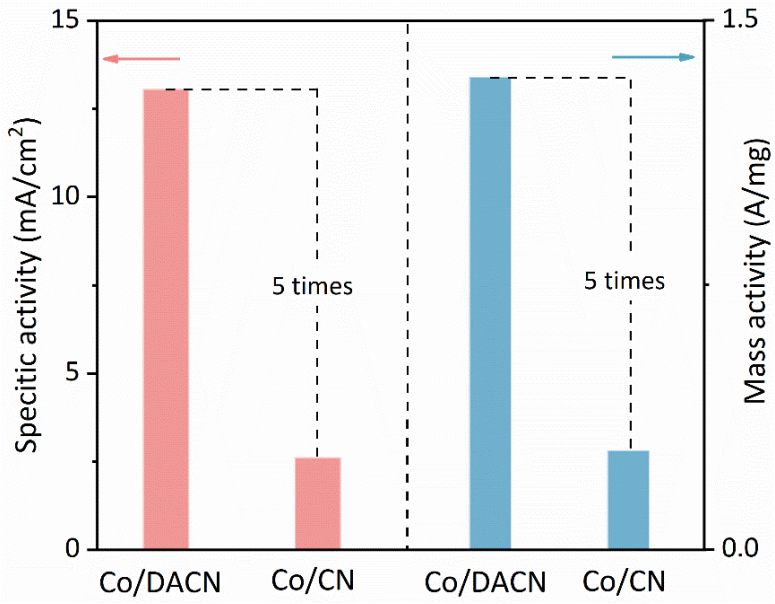

Fig. S24. Specific activity and mass activity of Co/CN and Co/DACN.

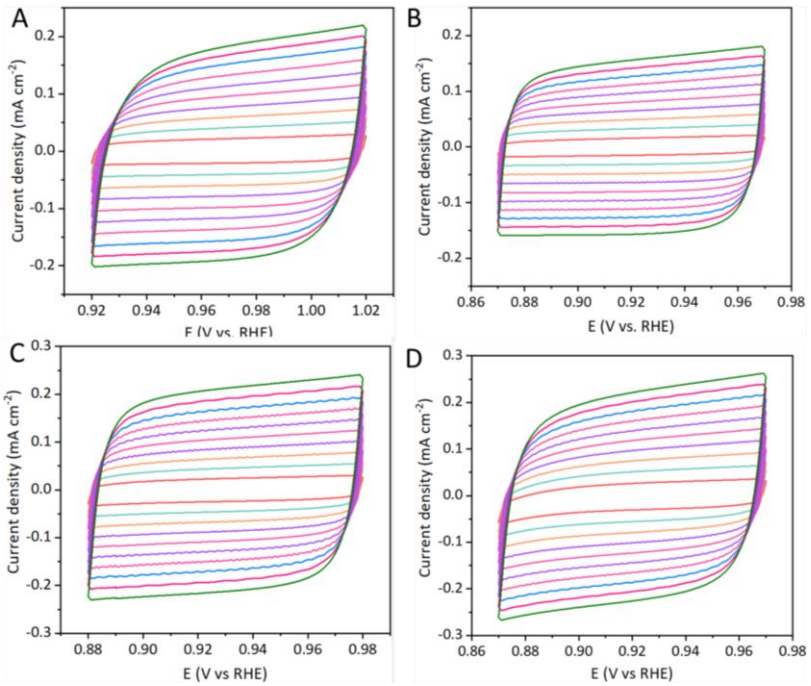

Fig. S25. CV curves of a) Pt/C, b) Zn/CN, c) Co/CN, and d) Co/DACN.

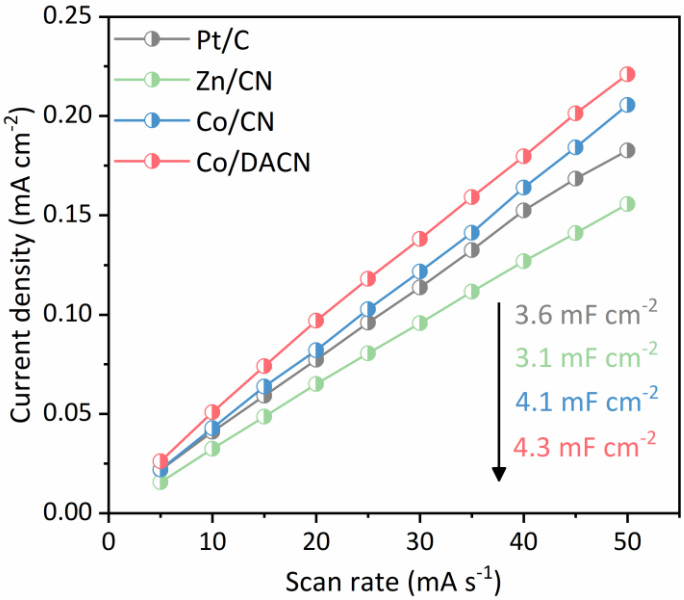

Fig. S26. The C_{dl} values over these catalysts from Fig. 25.

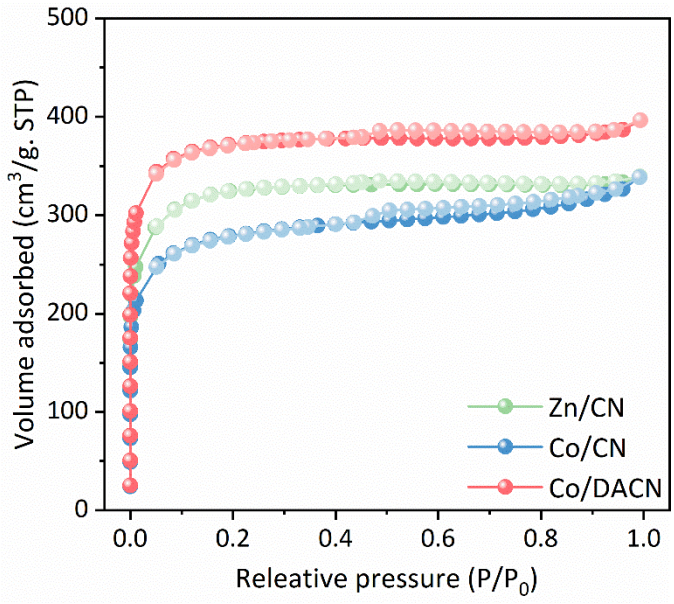

Fig. S27. Nitrogen adsorption-desorption isotherms of Zn/CN, Co/CN and Co/DACN.

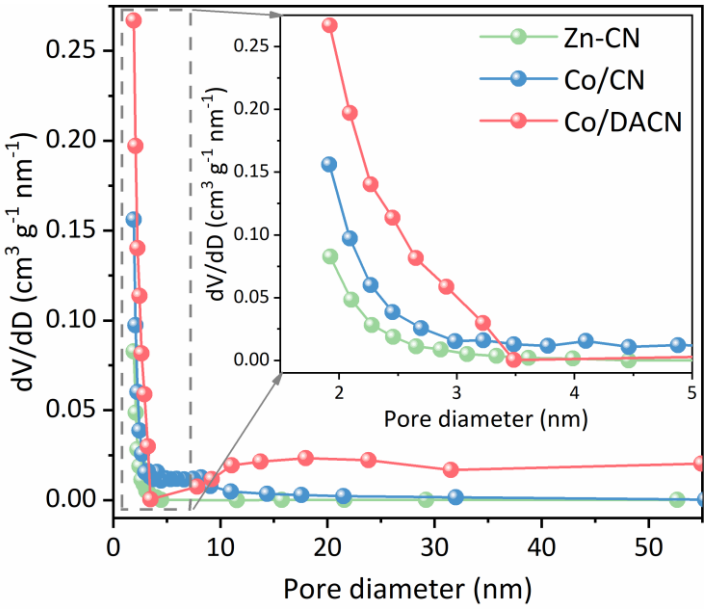

Fig. S28. BJH pore size distributions of Zn/CN, Co/CN and Co/DACN.

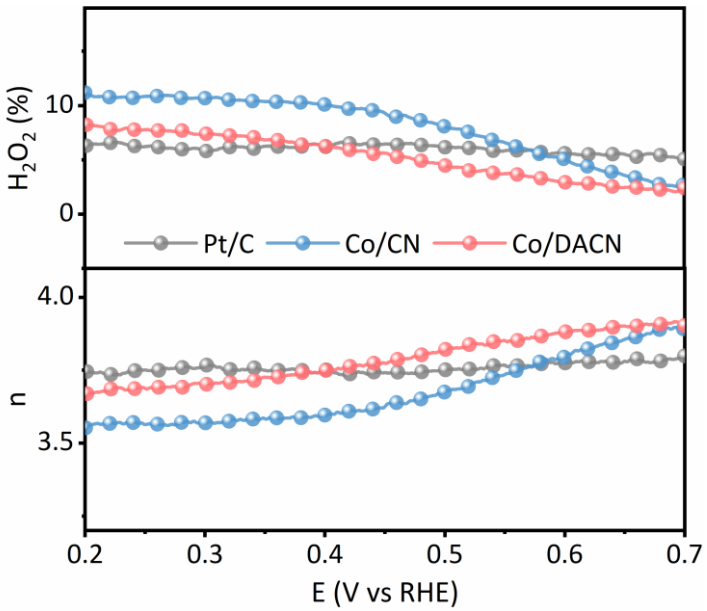

Fig. S29. Peroxide yield and the corresponding electron transfer number at different potentials.

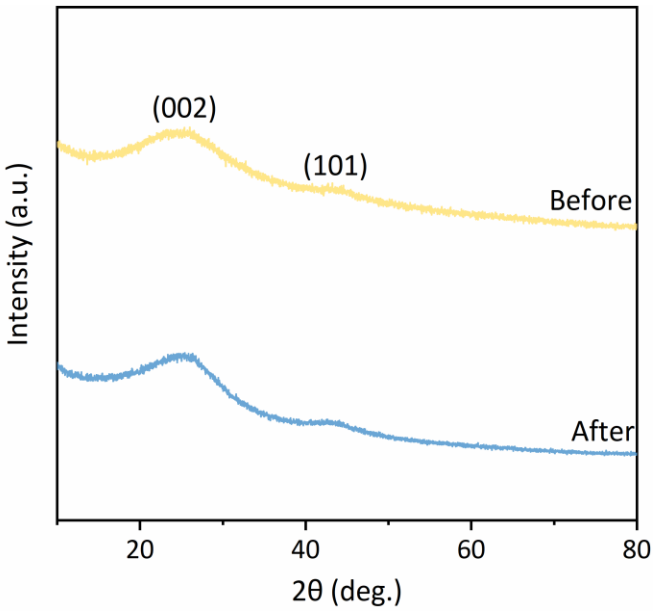

Fig. S30. The XRD patterns of Co/DACN before and after the ORR

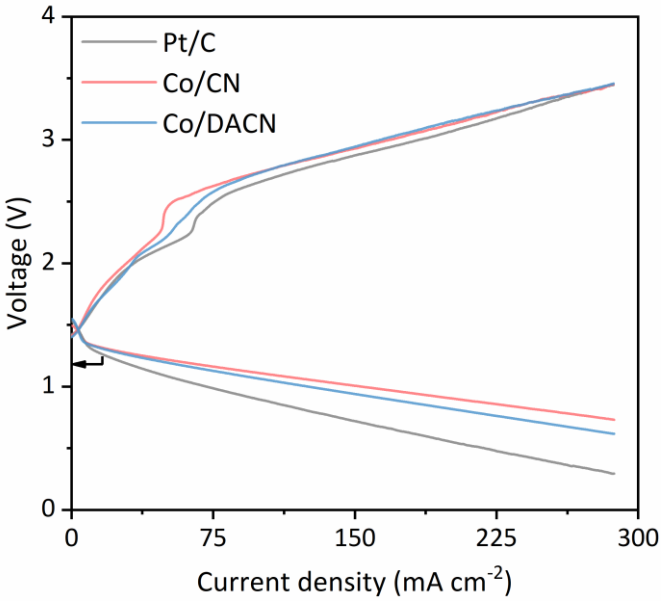

Fig. S31. Charge and discharge polarization curves of Zn-air batteries.

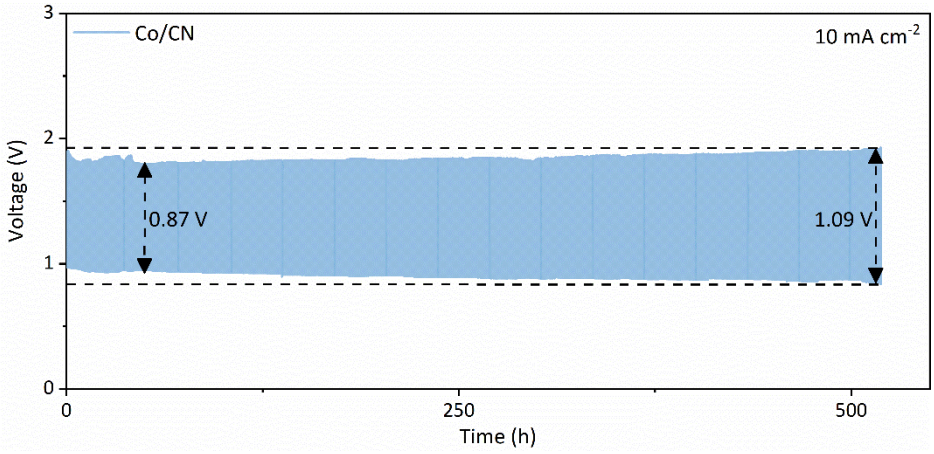

Fig. S32. Cycling performance of Co/CN at 10 mA cm^{-2}.

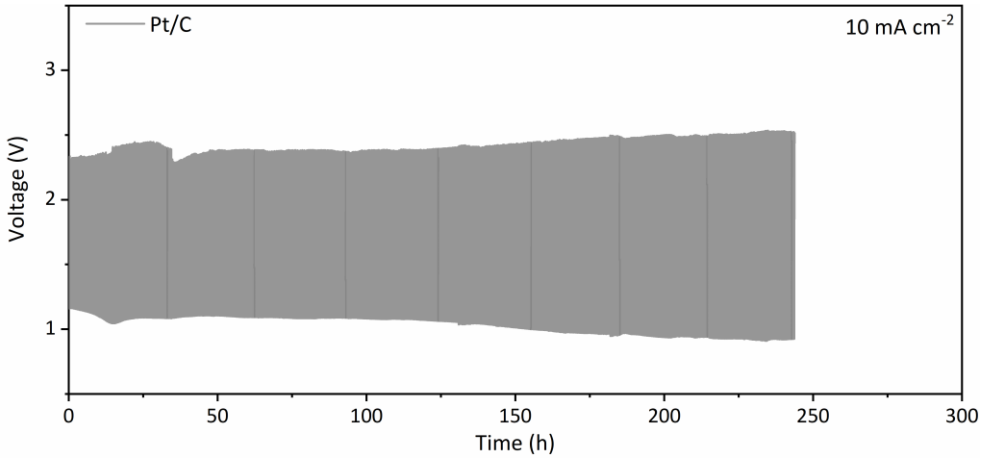

Fig. S33. Cycling performance of Pt/C at 10 mA cm^{-2}.

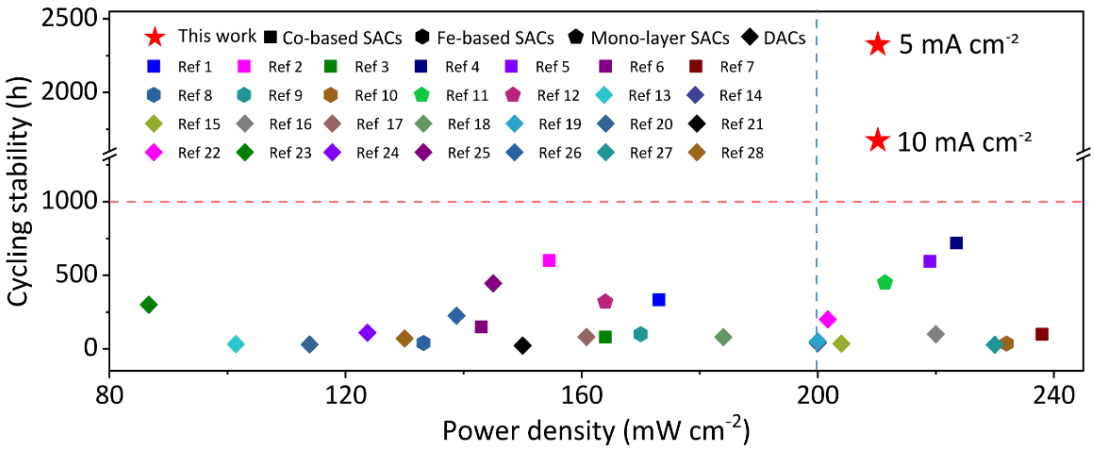

Fig. S34. Comparison of Zn-air battery performance using Co/DACN with the reported state-of-the-art catalysts.

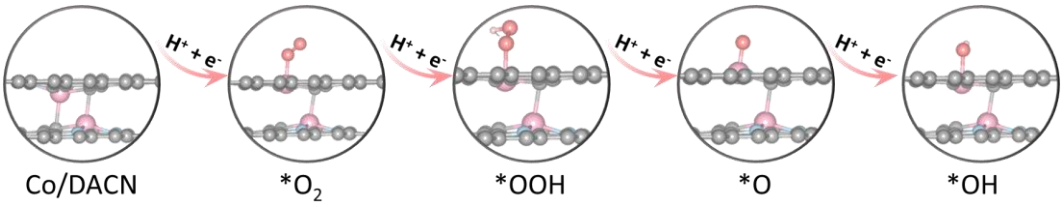

Fig. S35. Elementary steps of the ORR on Co/DACN in alkaline media.

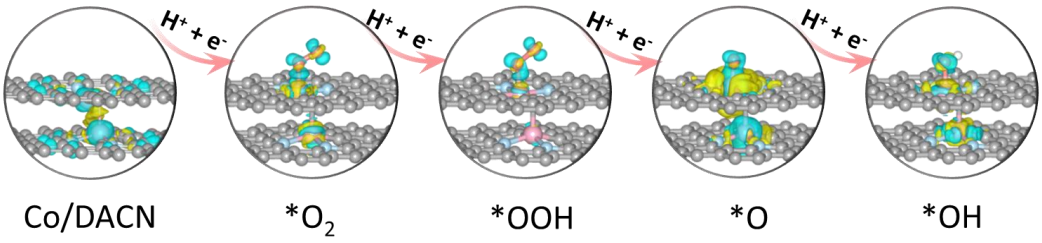

Fig. S36. Charge density difference on Co/DACN during the ORR process.

Table S1. Composition of all samples detected by ICP-MS measurements

Samples	**Zn wt.%**	**Co wt.%**
Zn/CN	8.89	---
Co/CN	5.04	4.37
Co/DACN	---	4.28

Table S2. The atomic ratio of C and N in all samples detected by XPS

Samples	**C/N**
Zn/CN	8.86
Co/CN	7.08
Co/DACN	29.53

Table S3. Chemical composition of Zn/CN obtained by XPS analysis

Elements	Assignment	Position (eV)
C	C-N	287.49
	C=N	285.47
	C-C	284.70
N	Oxidized N	402.90
	Graphitic N	401.07
	Pyrrolic N	399.78
	Pyridinic N	398.30
Zn	$2p_{1/2}$, $2p_{3/2}$	1044.40, 1021.30

Table S4. Chemical composition of Co/CN obtained by XPS analysis

Elements	Assignment	Position (eV)
C	C-N	288.15
	C=N	285.64
	C-C	284.64
N	Oxidized N	403.38
	Graphitic N	401.00
	Pyrrolic N	399.85
	Pyridinic N	398.40
Zn	$2p_{1/2}$, $2p_{3/2}$	1044.44, 1021.36
Co	$2p_{1/2}$, $2p_{3/2}$	795.70, 780.45

Table S5. Chemical composition of Co/DACN obtained by XPS analysis

Elements	Assignment	Position (eV)
C	C-N	287.58
	C=N	285.27
	C-C	284.70
N	Oxidized N	404.34
	Graphitic N	401.25
	Pyrrolic N	399.90
	Pyridinic N	398.53
Co	$2p_{1/2}$, $2p_{3/2}$	796.20, 780.88

Table S6. Structural parameters extracted from the EXAFS fitting

Sample	Bond	CN	R (Å)	**σ^2(10^{-3} Å^2)**	△E	χ_v^2 / R factor
Zn/CN	Zn-N	4.3	1.98(±0.069)	10.0(±0.013)	1.6	10.0/0.02
Co/CN	Co-N	4.4	1.93(±0.05)	10.0(±0.006)	-3.3	675.4/0.015
Co/DACN	Zn-N	4.2	2.04(±0.12)	6.8(±0.003)	7.0	12.6/0.0007
Co/DACN	Co-N	2.3	1.90(±0.10)	6.5(±0.007)	-2.8	259.2/0.016
	Co-C	2.9	2.12(±0.12)	6.5(±0.007)	-2.8	
Co foil	Co-Co	12	2.49(±0.0015)	6.1(±0.00018)	5.8	19.8/0.00066
Zn foil	Zn-Zn	6	2.63(±0.0051)	11.1(±0.00023)	3.5	21.7/0.0067

Note: The coordinated number Zn was about 4 in Co/CN and reference Zn/CN (Supplementary Table 6), which is similar to ZnPc.

Table S7. The onset potential and half-wave potential of ORR

Samples	Onset potential at 0.1 mA cm^{-2} (V vs RHE)	Half-wave potential (V vs RHE)
Co/DACN	0.95	0.85
Co/CN	0.93	0.82
Zn/CN	0.88	0.72
Pt/C	0.95	0.82

Table S8. The surface area, pore size and pore volume of these samples

Samples	Specific surface area ($m^2 g^{-1}$)	Pore volume ($cm^3 g^{-1}$)	Average pore size (nm)
Zn/CN	1013.04	0.05	2.91
Co/CN	1143.87	0.05	3.98
Co/DACN	1187.94	0.06	4.00

Table S9. Comparison of Zn-air battery performance between Co/DACN and the reported state-of-the-art catalysts

Catalysts	Voltage Gap (ΔE/V)	Power Density ($mW \cdot cm^{-2}$)	Stability	Ref.
Co/DACN	0.76 (5 mA cm^{-2}) 0.93 (10 mA cm^{-2})	210.1	2336 h (> 7000 cycles), 5 mA cm^{-2} 1688 h (5000 cycles), 10 mA cm^{-2}	This work
CoSA/N,S–HCS	0.82	173.1	~333 h (1000 cycles, 10 mA cm^{-2})	(10)
Co SA/NCFs	--	154.5	600 h, 10 mA^{-2}	(11)
CoHITP2	--	164	80 h, 5 mA^{-2}	(12)
Co-As/SNPs@NC	--	223.5	720 h (1080 cycles), 5 mA cm^{-2}	(13)
Co–CMS	0.77	219	594 h, 2 mA cm^{-2}	(14)
O–Co–N/C	0.722	143	150 h, 2 mA cm^{-2}	(15)
OLC/Co–N–C	0.8	238	100 h, 2 mA cm^{-2}	(16)
Fe–N/P–C–700	--	133.2	40 h, 10 mA cm^{-2}	(17)
FeN_4Cl_1	--	170	100 h, 10 mA cm^{-2}	(18)
Fe–N_4 SAs/NPC	--	232	36 h (108 cycles), 2 mA^{-2}	(19)
Bilayer Fe–N_x–C	--	211.4	450 h (2200 cycles), 10 mA cm^{-2}	(20)
Bilayer Fe–N_5	--	164	320 h, 10 mA cm^{-2}	(21)
CoNi–SAs/CN	0.82	101.4	~32 h (95 cycles), 5 mA cm^{-2}	(22)
Fe–N_4/Pt–N_4@NC	--	~ 200	40 h, 10 mA cm^{-2}	(23)
PtCo–NC	--	204	35 h,10 mA cm^{-2}	(24)
Fe–NiNC-50	0.86	220	100 h (600 cycles), 10 mA^{-2}	(25)
Fe,Mn/N–C	--	160.8	81 h, 5 mA^{-2}	(26)
FeMn–DSAC	0.71	184	80 h, 2 mA^{-2}	(27)
BTC–Co–O–Cu–BTA MOF	--	200	50 h (50 cycles), 50 mA^{-2}	(28)
IrFe−N−C cathode	--	113.9	30 h (60 cycles), 5 mA^{-2}	(29)
(Zn,Co)/NSC	--	150	22 h, 5 mA^{-2}	(30)
Fe_1Co_1–CNF	1.01	201.7	200 h (600 cycles), 20 mA^{-2}	(31)
(Fe,Co) –SA/CS	0.88	86.65	300 h (900 cycles), 5 mA^{-2}	(32)
ZnCo–HNC	--	123.7	110 h, 5 mA^{-2}	(33)
CoFeN-NCNTs//CCM	0.76	145	445 h (1335 cycles) 10 mA cm^{-2}	(34)
IrCo−N−C	0.701	138.8	225 h (450 cycles) 5 mA cm^{-2}	(35)
Zn/CoN–C	--	230	27.7 h, 5 mA cm^{-2}	(36)
$RuCoN_x$/C electrode	0.603	130	70 h (140 cycles), 2 mA cm^{-2}	(37)

SI References

1. Y. L. Wu, X. F. Li, Y. S. Wei, Z. M. Fu, W. B. Wei, X. T. Wu, Q. L. Zhu, Q. Xu, Ordered microporous superstructure of nitrogen-doped nanoporous carbon implanted with ultrafine Ru nanoclusters for efficient pH-universal hydrogen evolution reaction. *Adv. Mater.* **33**, e2006965 (2021).
2. Z. Song, L. Zhang, K. Doyle-Davis, X. Fu, J. L. Luo, X. Sun, Recent advances in MOF-derived single atom catalysts for electrochemical applications. *Adv. Energy Mater.* **10**, 2001561 (2020).
3. G. Henkelman, B. P. Uberuaga, H. Jónsson, A climbing image nudged elastic band method for finding saddle points and minimum energy paths. *J. Chem. Phys.* **113**, 9901-9904 (2000).
4. K. L. Zhou, Z. Wang, C. B. Han, X. Ke, C. Wang, Y. Jin, Q. Zhang, J. Liu, H. Wang, H. Yan, Platinum single-atom catalyst coupled with transition metal/metal oxide heterostructure for accelerating alkaline hydrogen evolution reaction. *Nat. Commun.* **12**, 3783 (2021).
5. J. P. Perdew, K. Burke, M. Ernzerhof, Generalized gradient approximation made simple. *Phys. Rev. Lett.* **77**, 3865 (1996).
6. G. Kresse, J. Furthmüller, Efficient iterative schemes for ab initio total-energy calculations using a plane-wave basis set. *Phys. Rev. B* **54**, 11169-11186 (1996).
7. P. E. Blöchl, Projector augmented-wave method. *Phys. Rev. B* **50**, 17953 (1994).
8. G. Kresse, D. Joubert, From ultrasoft pseudopotentials to the projector augmented-wave method. *Phys. Rev. B* **59**, 1758 (1999).
9. J. K. Nørskov, J. Rossmeisl, A. Logadottir, L. Lindqvist, J. R. Kitchin, T. Bligaard, H. Jónsson, Origin of the overpotential for oxygen reduction at a fuel-cell cathode. *J. Phys. Chem. B* **108**, 17886-17892 (2004).
10. Z. Y. Zhang, X. X. Zhao, S. B. Xi, L. L. Zhang, Z. X. Chen, Z. P. Zeng, M. Huang, H. B. Yang, B. Liu, S. J. Pennycook, P. Chen, Atomically dispersed cobalt trifunctional electrocatalysts with tailored coordination environment for flexible rechargeable Zn–air battery and self‐driven water splitting. *Adv. Energy Mater.* **10**, 2002896-2002906 (2020).
11. Y. Han, H. Duan, C. Zhou, H. Meng, Q. Jiang, B. Wang, W. Yan, R. Zhang, Stabilizing cobalt single atoms via flexible carbon membranes as bifunctional electrocatalysts for binder-free zinc-air batteries. *Nano Lett.* **22**, 2497-2505 (2022).
12. Y. B. Lian, W. J. Yang, C. F. Zhang, H. Sun, Z. Deng, W. J. Xu, L. Song, Z. W. Ouyang, Z. X. Wang, J. Guo, Y. Peng, Unpaired 3d electrons on atomically dispersed cobalt centres in coordination polymers regulate both oxygen reduction reaction (ORR) activity and selectivity for use in zinc-air batteries. *Angew. Chem., Int. Ed.* **59**, 286-294 (2020).
13. Z. Wang, C. Zhu, H. Tan, J. Liu, L. Xu, Y. Zhang, Y. Liu, X. Zou, Z. Liu, X. Lu, Understanding the synergistic effects of cobalt single atoms and small nanoparticles: enhancing oxygen reduction reaction catalytic activity and stability for zinc-air batteries. *Adv. Funct. Mater.* **31**, 2104735 (2021).
14. S. Liang, L. C. Zou, L. J. Zheng, F. Li, X. X. Wang, L. N. Song, J. J. Xu, Highly stable Co single atom confined in hierarchical carbon molecular sieve as efficient electrocatalysts in metal-air batteries. *Adv. Funct. Mater.* **12**, 2103097 (2022).
15. W. Zhang, C. H. Xu, H. Zheng, R. Li, K. Zhou, Oxygen-rich cobalt-nitrogen-carbon porous nanosheets for bifunctional oxygen electrocatalysis. *Adv. Funct. Mater.* **32**, 2200763 (2022).
16. Z. Liang, N. Kong, C. Yang, W. Zhang, H. Zheng, H. Lin, R. Cao, Highly curved nanostructure-coated Co, N-doped carbon materials for oxygen electrocatalysis. *Angew. Chem., Int. Ed.* **60**, 12759-12764 (2021).
17. K. Yuan, D. Lützenkirchen-Hecht, L. Li, L. Shuai, Y. Li, R. Cao, M. Qiu, X. Zhuang, M. K. H. Leung, Y. Chen, U. Scherf, Boosting oxygen reduction of single iron active sites via geometric and electronic engineering: nitrogen and phosphorus dual coordination. *J. Am. Chem. Soc.* **142**, 2404-2412 (2020).
18. L. Hu, C. Dai, L. Chen, Y. Zhu, Y. Hao, Q. Zhang, L. Gu, X. Feng, S. Yuan, L. Wang, B. Wang, Metal-triazolate-framework-derived FeN_4Cl_1 single-atom catalysts with hierarchical porosity for the oxygen reduction reaction. *Angew. Chem., Int. Ed.* **60**, 27324-27329 (2021).
19. Y. Pan, S. J. Liu, K. A. Sun, X. Chen, B. Wang, K. L. Wu, X. Cao, W. C. Cheong, R. G. Shen, A. J. Han, Z. Chen, L. R. Zheng, J. Luo, Y. Lin, Y. Q. Liu, D. S. Wang, Q. Peng, Q. Zhang, C. Chen, Y. D. Li, A bimetallic Zn/Fe polyphthalocyanine-derived single-atom Fe-N_4 catalytic site: a superior trifunctional catalyst for overall water splitting and Zn-air batteries. *Angew. Chem., Int. Ed.* **57**, 8614-8618 (2018).
20. X. Wu, Q. Wang, S. Yang, J. Zhang, Y. Cheng, H. Tang, L. Ma, X. Min, C. Tang, S. P. Jiang, F. Wu, Y. Lei, S. Ciampic, S. Wang, L. Dai, Sublayer-enhanced atomic sites of single atom

catalysts through in situ atomization of metal oxide nanoparticles. *Energy Environ. Sci.* **15**, 1183-1191 (2022).
21. X. Liang, Z. Li, H. Xiao, T. Zhang, P. Xu, H. Zhang, Q. Gao, L. Zheng, Two types of single-atom FeN_4 and FeN_5 electrocatalytic active centers on N-doped carbon driving high performance of the SA-Fe-NC oxygen reduction reaction catalyst. *Chem. Mater.* **33**, 5542-5554 (2021).
22. X. Han, X. Ling, D. Yu, D. Xie, L. Li, S. Peng, C. Zhong, N. Zhao, Y. Deng, W. Hu, Atomically dispersed binary Co-Ni sites in nitrogen-doped hollow carbon nanocubes for reversible oxygen reduction and evolution. *Adv. Mater.* **31**, 1905622 (2019).
23. A. Han, X. Wang, K. Tang, Z. Zhang, C. Ye, K. Kong, H. Hu, L. Zheng, P. Jiang, C. Zhao, Q. Zhang, D. Wang, Y. Li, An adjacent atomic platinum site enables single-atom iron with high oxygen reduction reaction performance. *Angew. Chem., Int. Ed.* **60**, 19262-19271 (2021).
24. Y. Cheng, X. Gong, S. Tao, L. Hu, W. Zhu, M. Wang, J. Shi, F. Liao, H. Geng, M. Shao, Mechano-thermal milling synthesis of atomically dispersed platinum with spin polarization induced by cobalt atoms towards enhanced oxygen reduction reaction. *Nano Energy* **98**, 107341 (2022).
25. X. Zhu, D. Zhang, C.-J. Chen, Q. Zhang, R.-S. Liu, Z. Xia, L. Dai, R. Amal, X. Lu, Harnessing the interplay of Fe-Ni atom pairs embedded in nitrogen-doped carbon for bifunctional oxygen electrocatalysis. *Nano Energy* **71**, 104597 (2020).
26. G. Yang, J. Zhu, P. Yuan, Y. Hu, G. Qu, B.-A. Lu, X. Xue, H. Yin, W. Cheng, J. Cheng, W. Xu, J. Li, J. Hu, S. Mu, J.-N. Zhang, Regulating Fe-spin state by atomically dispersed Mn-N in Fe-NC catalysts with high oxygen reduction activity. *Nat. Commun.* **12**, 1734 (2021).
27. T. Cui, Y. P. Wang, T. Ye, J. Wu, Z. Chen, J. Li, Y. Lei, D. Wang, Y. Li, Engineering dual single-atom sites on 2D ultrathin N-doped carbon nanosheets attaining ultra-low-temperature zinc-air battery. *Angew. Chem., Int. Ed.* **61**, e202115219 (2022).
28. M. F. Sanad, A. R. Puente Santiago, S. A. Tolba, M. A. Ahsan, O. Fernandez-Delgado, M. Shawky Adly, E. M. Hashem, M. Mahrous Abodouh, M. S. El-Shall, S. T. Sreenivasan, N. K. Allam, L. Echegoyen, Co-Cu bimetallic metal organic framework catalyst outperforms the Pt/C benchmark for oxygen reduction. *J. Am. Chem. Soc.* **143**, 4064-4073 (2021).
29. Z. Yu, C. Si, A. P. LaGrow, Z. Tai, W. A. Caliebe, A. Tayal, M. J. Sampaio, J. P. S. Sousa, I. Amorim, A. Araujo, L. Meng, J. L. Faria, J. Xu, B. Li, L. Liu, Iridium-iron diatomic active sites for efficient bifunctional oxygen electrocatalysis. *ACS Catal.* **12**, 9397-9409 (2022).
30. D. Liu, B. Wang, H. Li, S. Huang, M. Liu, J. Wang, Q. Wang, J. Zhang, Y. Zhao, Distinguished Zn, Co-Nx-C-Sy active sites confined in dentric carbon for highly efficient oxygen reduction reaction and flexible Zn-air Batteries. *Nano Energy* **58**, 277-283 (2019).
31. Y. Wang, Z. Li, P. Zhang, Y. Pan, Y. Zhang, Q. Cai, S. R. P. Silva, J. Liu, G. Zhang, X. Sun, Flexible carbon nanofiber film with diatomic Fe-Co sites for efficient oxygen reduction and evolution reactions in wearable zinc-air batteries. *Nano energy* **87**, 106147 (2021).
32. G. Zhou, G. Liu, X. Liu, Q. Yu, H. Mao, Z. Xiao, L. Wang, 1D/3D Heterogeneous assembling body as trifunctional electrocatalysts enabling zinc-air battery and self-powered overall water splitting. *Adv. Funct. Mater.* **32**, 2107608 (2022).
33. S. Y. Lin, L. X. Xia, Y. Cao, H. L. Meng, L. Zhang, J. J. Feng, Y. Zhao, A. J. Wang, Electronic regulation of ZnCo dual-atomic active sites entrapped in 1D@2D hierarchical N-doped carbon for efficient synergistic catalysis of oxygen reduction in Zn-air battery.*Small*, **18**, 2107141 (2022).
34. V. Jose, H. Hu, E. Edison, W. Manalastas Jr, H. Ren, P. Kidkhunthod, S. Sreejith, A. Jayakumar, J. M. V. Nsanzimana, M. Srinivasan, J. Choi, J. Lee, Modulation of single atomic Co and Fe sites on hollow carbon nanospheres as oxygen electrodes for rechargeable Zn-air batteries. *Small Methods* **5**, 2000751 (2021)
35. M. Xiao, J. Zhu, S. Li, G. Li, W. Liu, Y. P. Deng, Z. Bai, L. Ma, M. Feng, T. Wu, D. Su, J. Lu, A. Yu, Z. Chen, 3D-orbital occupancy regulated Ir-Co atomic pair toward superior bifunctional oxygen electrocatalysis. *Acs Catal.* **11**, 8837-8846 (2021).
36. Z. Lu, B. Wang, Y. Hu, W. Liu,. Y. Zhao, R. Yang, Z. Li, J. Luo, B. Chi, Z. Jiang, M. Li, S. Mu, S. Liao, J. Zhang, X. Sun, An isolated zinc-cobalt atomic pair for highly active and durable oxygen reduction. *Angew. Chem., Int. Ed.* **58**, 2622-2626 (2019).
37. M. Liu, H. Chun, T.-C. Yang, S. J. Hong, C.-M. Yang, B. Han, L. Y. S. Lee, Tuning the site-to-site interaction in Ru-M (M = Co, Fe, Ni) diatomic electrocatalysts to climb up the volcano plot of oxygen electroreduction. *ACS Nano* **16**, 10657-10666 (2022).